The Astrophysical Journal, 719:1350–1361, 2010 August 20 doi:10.1088/0004-637X/719/2/1350

SUZAKU AND *BeppoSAX* X-RAY SPECTRA OF THE PERSISTENTLY ACCRETING NEUTRON-STAR BINARY 4U 1705-44

Dacheng Lin[1,2], Ronald A. Remillard[1], and Jeroen Homan[1]

[1] MIT Kavli Institute for Astrophysics and Space Research, MIT, 70 Vassar Street, Cambridge, MA 02139-4307, USA

[2] Centre d'Etude Spatiale des Rayonnements, 9, av du Colonel Roche, BP 44346, 31028 Toulouse Cedex 4, France; Dacheng.Lin@cesr.fr

Received 2009 September 1; accepted 2010 June 24; published 2010 July 28

ABSTRACT

We present an analysis of the broadband spectra of 4U 1705–44 obtained with *Suzaku* in 2006–2008 and by *BeppoSAX* in 2000. The source exhibits two distinct states: the hard state shows emission from 1 to 150 keV, while the soft state is mostly confined to be <40 keV. We model soft-state continuum spectra with two thermal components, one of which is a multicolor accretion disk and the other is a single-temperature blackbody (BB) to describe the boundary layer, with additional weak Comptonization represented by either a simple power law or the SIMPL model by Steiner et al. The hard-state continuum spectra are modeled by a single-temperature BB for the boundary layer plus strong Comptonization, modeled by a cutoff power law. While we are unable to draw firm conclusions about the physical properties of the disk in the hard state, the accretion disk in the soft state appears to approximately follow $L \propto T^{3.2}$. The deviation from $L \propto T^4$, as expected from a constant inner disk radius, might be caused by a luminosity-dependent spectral hardening factor and/or real changes of the inner disk radius in some part of the soft state. The boundary layer apparent emission area is roughly constant from the hard to the soft states, with a value of about 1/11 of the neutron star surface. The magnetic field on the surface of the neutron star in 4U 1705–44 is estimated to be less than about 1.9×10^8 G, assuming that the disk is truncated by the innermost stable circular orbit or by the neutron star surface. Broad relativistic Fe lines are detected in most spectra and are modeled with the diskline model. The strength of the Fe lines is found to correlate well with the boundary layer emission in the soft state. In the hard state, the Fe lines are probably due to illumination of the accretion disk by the strong Comptonization emission.

Key words: accretion, accretion disks – stars: neutron – X-rays: binaries – X-rays: bursts – X-rays: stars

Online-only material: color figures

1. INTRODUCTION

There are two main classes of luminous and weakly magnetized neutron stars (NSs) in low-mass X-ray binaries (LMXBs), i.e., atoll and Z sources, named after the patterns that they trace out in X-ray color–color diagrams (CDs) or hardness-intensity diagrams (HIDs; Hasinger & van der Klis 1989; van der Klis 2006). Atoll sources have lower luminosities (∼0.001–0.5 $L_{\rm Edd}$) than Z sources, and have two distinct X-ray states, i.e., hard (energy spectra are roughly flat with power-law photon index near 1.7) and soft states (energy spectra follow exponential decrease above ∼10 keV). There is also a "transitional" state between these two. The hard, transitional, and soft states of atoll sources are also often referred to as the "extreme island," "island," and "banana" states/branches, respectively. Z sources only have soft spectra, but there are three distinct branches with different spectral and timing behaviors. Recently, Lin et al. (2009) and Homan et al. (2010) analyzed a transiently accreting NS, XTE J1701-462, which changed from Z-source behavior to atoll-source characteristics as the outburst decayed from near/super Eddington luminosity ($L_{\rm Edd}$) to almost quiescence. These results confirmed that the differences in the properties of the two classes are due to their different mass accretion rates. The spectral modeling of NS LMXBs has been controversial for a long time (see Barret 2001 for a review). The continuum of soft-state spectra in both atoll and Z sources are generally described by two-component models that include a soft/thermal and a hard/Comptonized component (e.g., Barret et al. 2000; Oosterbroek et al. 2001; Di Salvo et al. 2000; Iaria et al. 2005), and there have been two competing models, often referred to as the *Eastern* model (after Mitsuda et al. 1989) and the *Western* model (after White et al. 1988), with different choices of the thermal and Comptonized components. In the *Eastern* model, the thermal and Comptonized components are described by a multicolor disk blackbody (MCD) and a Comptonized blackbody (BB), respectively. In the *Western* model, on the other hand, the thermal component is a single-temperature BB from the boundary layer, and there is Comptonized emission from the disk. In the hard state, the spectra are dominated by a hard/Comptonized component, but a soft/thermal component is generally still required (Christian & Swank 1997; Barret et al. 2000; Church & Balucińska-Church 2001; Gierliński & Done 2002). Lin et al. (2007) implemented the commonly used two-component models for two classical transient atoll sources, i.e., Aql X-1 and 4U 1608-52, and outlined the problem of model degeneracy for accreting NSs, not only from the choices of the thermal components, but also from the detailed description of Comptonized components (i.e., the scattering corona geometry, the seed photon temperature, etc.). The physical interpretation of the spectral evolution of these atoll sources inferred from these different models also varies substantially. However, none of the tested models produced results similar to those of black hole X-ray binaries, i.e., $L_{\rm X} \propto T^4$ tracks for the MCD component and weak Comptonization for the soft-state spectra when the integrated rms variability in the power density spectrum (0.1–10 Hz) is only a few percent (Remillard & McClintock 2006).

Lin et al. (2007) devised a hybrid model for atoll sources, based on a detailed study of two frequently recurring atoll-type transients. This model uses a BB to describe the boundary layer plus a broken power law for the hard state, and two strong

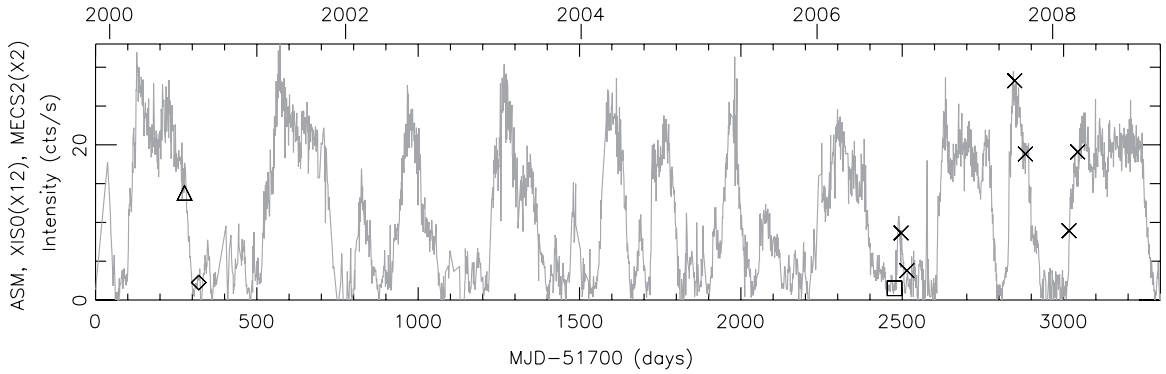

Figure 1. Long-term *RXTE*/ASM light curve of 4U 1705–44. The various symbols represent different spectral states from different pointed observatories: *BeppoSAX*/*Suzaku* hard state (diamond/square) and *BeppoSAX*/*Suzaku* soft state (triangle/cross).

thermal components (MCD and BB) plus a constrained broken power law (when needed) for the soft state. This choice for the soft state offers a weak-Comptonization solution that differs from the strong-Comptonization solution of the two-component models that had previously dominated the literature. The results of the application of the hybrid model can be summarized as follows: both the MCD and BB evolve approximately as $L_X \propto T^4$, the spectral/timing correlations of these NSs are aligned with the properties of accreting black holes, and the visible BB emission area is very small but roughly constant over a wide range of L_X that spans both the hard and soft states. Lin et al. (2009) applied this X-ray spectral model to XTE J1701-462, and similar results were obtained for the observations when the source displayed atoll-source behavior. Deviations of the MCD from the $L_X \propto T^4$ track were observed when the source was bright and behaved as a Z source, with the inner disk showing a luminosity-dependent radius increase. This was interpreted as an effect of maintaining the local Eddington limit in the inner disk edge as the mass accretion rate varies.

The hybrid spectral model is still empirical, especially the modeling of Comptonization. Moreover, this model has only been applied thus far to extensive data obtained with the *Rossi X-ray Timing Explorer* (*RXTE*). *RXTE* has two pointing instruments, which cover the energy range from ∼2.5 to 250 keV. However, there is emission from X-ray binaries below this energy range, as the characteristic temperatures of the thermal components are normally below 3 keV. Thus, it is important to test this model using broadband spectra that extend to photon energies below the sensitivity range of *RXTE*.

In this paper, we investigate the persistently bright atoll source, 4U 1705-44 (Hasinger & van der Klis 1989), which was observed seven times in 2006–2008 by *Suzaku* (Mitsuda et al. 2007). One of the important features of *Suzaku* is its broad energy band (0.2–600 keV). We also analyzed two observations of 4U 1705-44 made with *BeppoSAX* (0.1–300 keV) in 2000. Both *Suzaku* and *BeppoSAX* additionally provide better energy resolutions than *RXTE* (∼2%, 8%, 18% at 6 keV (FWHM), respectively), and this capability can be used to better resolve the broad Fe emission lines. Broad Fe lines are commonly seen in X-ray binaries and provide another tool for investigating the accretion flow around compact objects (e.g., Miller 2007; Cackett et al. 2008, 2009b).

Timing studies for 4U 1705-44, including the findings of kilohertz quasi-periodic oscillations (kHz QPOs), have been carried out using observations with *RXTE* (Ford et al. 1998; Barret & Olive 2002; Olive et al. 2003). Spectral studies of this source have also been carried out, using different kinds of X-ray detectors and spectral models (e.g., Barret & Olive 2002; Di Salvo et al. 2005; Fiocchi et al. 2007; Piraino et al. 2007; Homan et al. 2009; Reis et al. 2009; di Salvo et al. 2009). Several of these authors also reported the detection of a broad relativistic Fe line from this source. In this paper, we concentrate on the spectral properties of this source. We describe our data analysis in Section 2, where we also present the long-term light curves and CDs. We perform detailed spectral modeling in Section 3, for which we provide our physical interpretations in Section 4. Finally, we give our summary and discussion.

2. OBSERVATIONS AND DATA REDUCTION

The long-term light curve of 4U 1705-44 is shown in Figure 1. The gray solid line is from the *RXTE* All-Sky Monitor (ASM; Levine et al. 1996), and we can see that the source displays persistent X-ray emission, with one or two strong intensity cycles per year. These cycles correspond to state-transition cycles (Homan et al. 2009). Discrete plot symbols show the time and spectral states during different pointed observations. The data reduction and spectral analyses are described below.

2.1. Suzaku Data

Suzaku made seven observations of 4U 1705-44 in 2006–2008. Detailed information of these observations is given in Table 1. Both the X-ray Imaging Spectrometer (XIS, 0.2–12 keV; Koyama et al. 2007) and the Hard X-ray Detector (HXD, 10–600 keV; Takahashi et al. 2007) instruments were used during these observations. There are four XIS detectors, numbered as 0 to 3. XIS0, 2, and 3 all use front-illuminated CCDs and have very similar responses, while XIS1 uses a back-illuminated CCD. XIS2 was damaged in 2006 November, and its data are analyzed only for the first three observations. The HXD instrument includes both PIN diodes (10–70 keV) and GSO scintillators (30–600 keV). Both the PIN and GSO are collimated (non-imaging) instruments.

We reprocessed each observation using the `aepipeline` tool provided by *Suzaku* FTOOLS version 15 and applying the latest calibration available as of 2010 February. We then applied the publicly available tool `aeattcor.sl` by John E. Davis to obtain a new attitude file for each observation. This tool corrects the effects of thermal flexing of the *Suzaku* spacecraft and obtains more accurate estimate of the spacecraft attitude. For all our seven observations, the above attitude correction produced sharper point-spread function (PSF) images. With the new attitude file, we updated the XIS event files using the FTOOLS `xiscoord` program.

Table 1
Suzaku Observations of 4U 1705–44 in 2006–2008

Observation ID	401046010	401046020	401046030	402051010	402051020	402051030	402051040
Spectral ID	*suz*1	*suz*2	*suz*3	*suz*4	*suz*5	*suz*6	*suz*7
Observations							
Observation date	2006 Aug 29	2006 Sep 18	2006 Oct 06	2007 Sep 05	2007 Oct 08	2008 Feb 20	2008 Mar 18
Exposure of XIS/PIN (ks)[a]	10.9/12.8	12.7/12.1	13.3/12.4	2.2/8.2	3.9/14.5	18.4/17.3	3.0/11.1
XIS detectors analyzed	0 1 2 3	0 1 2 3	0 1 2 3	0 1 3	0 1 3	0 1 3	0 1 3
Window option	1/4	1/4	1/4	1/4	1/4	1/4	1/4
Exposure in burst option (s)	1.6	2.0	2.0	0.5	0.5	2.0	0.5
XIS0 count rate (counts s^{-1})[b]	18.1	103.7	45.5	339.2	225.9	107.1	229.0
Soft color[c]	0.81 ± 0.03	0.72 ± 0.02	0.64 ± 0.02	0.81 ± 0.03	0.73 ± 0.02	0.66 ± 0.02	0.79 ± 0.03
Hard color[c]	0.34 ± 0.03	0.11 ± 0.01	0.09 ± 0.01	0.08 ± 0.01	0.08 ± 0.01	0.09 ± 0.01	0.09 ± 0.01
Radius of central region							
With >5% pile-up (pixels)	0	55	32	52	39	60	35
Radius of central region							
With >10% pile-up (pixels)	0	39	21	35	24	42	24
Spectral state	Hard	Soft	Soft	Soft	soft	soft	soft

Notes.
[a] The dead time and burst clock options have been taken into account. All XIS detectors have the same exposure time, and the values given are for one detector only.
[b] Total time-averaged count rates, corresponding to the fully integrated PSF.
[c] The average and standard deviation of the colors for each observation based on 128s data bins.

Since 4U 1705-440 is a relatively bright source, window and burst options were adopted during each observation to limit the effects of event pile-up (Table 1). Despite this, pile-up was still present in the image center. We estimated the pile-up fractions at different positions of the CCD using the publicly available tool `pileup_estimate.sl` by Michael A. Nowak. The pile-up fraction refers to the ratio of events lost via grade or energy migration to the events expected in the absence of pile-up. The unfiltered pile-up fractions integrated over the whole CCDs are about 10%–15% for all observations except for the observation 401046010 (∼3%). Table 1 lists the radii of the central circular regions that contain most of the XIS CCD pixels with local pile-up fractions that exceed 5% and 10%, respectively. We used annular regions to extract spectra (circular regions are used for observation 401046010). The outer radius was set to be 120 pixels, while two cases of inner radii were used, corresponding to the 5% and 10% pile-up exclusion regions, respectively. The corresponding integrated pile-up fractions of all annular regions are ∼3% and ∼5%, respectively. Using the models for the soft-state spectra, which include MCD and BB components, we find that the spectral fitting results using 10% pile-up exclusion regions show systematic decrease in the soft-component (MCD) flux and increase in the hard-component (BB) flux, by about 3%, compared with the results using 5% pile-up exclusion regions. The differences in most cases are within the error bars at a 90% confidence level, and the conclusions of this paper hold for either case. For simplicity and increased accuracy, we only show results using the 5% pile-up exclusion regions below.

4U 1705-44 is in the direction toward the Galactic ridge, and the background consists of non-X-ray (particle) background, absorbed cosmic X-ray background, and Galactic ridge emission. Even though our source can be regarded as a point source, there is no region of the detector plane that is free from the source emission to estimate the pure background. This is because the PSF of the XIS is quite spread out and our source during these seven observations was bright enough to dominate over the background (1–10 keV) throughout the 1/4 window. We compared results using two methods of estimating the background. In the first method, we set the background region to be the whole 1/4 window excluding a circular region of radius 350″ around the source. In the second method, we estimated the non-X-ray background, which varies with time, using the `xisnxbgen` tool based on the night Earth data by *Suzaku*. We estimated the X-ray background, including the cosmic X-ray background and Galactic ridge emission, using observation 100026030 by *Suzaku*. It is specific for observing the background emission around the supernova remnant RX J1713-3946, and the pointing direction of this observation has a 184″ offset from 4U 1705-44. Both of the methods turn out to give very similar spectral fit results, and we only show results using the second method below.

The response files of the XIS for each observation were generated using the `xisresp` script which uses the `xisrmfgen` and `xissimarfgen` tools (specifying 1% accuracy). They take into account the time variation of the energy response and the specific extraction region for each observation and each XIS detector. As the responses of XIS0, 2, and 3 on the whole are very similar, we combined their spectra and responses using the script `addascaspec`.

We also extracted the PIN spectra. The non X-ray and cosmic X-ray backgrounds are taken into account. The non X-ray background is calculated from the background event files distributed by the HXD team. The cosmic X-ray background is from the model by Boldt (1987), and its flux is about 5% of the background for PIN. The response files provided by the HXD team were used. The GSO data were not used, considering the large uncertainty in calibration and low signal-to-noise ratios above 40 keV.

The CD/HID of these observations are shown in Figure 2. We defined soft and hard colors as the ratios of the count rates in the (3.6–5.0)/(2.2–3.6) keV bands and the (11.0–20.0)/(5.0–8.6) keV bands, respectively. The count rates of the lowest three energy bands were from XIS0, 1, and 3 combined. We first obtained the count rates using the 5% pile-up exclusion regions and then converted to the value corresponding to the whole integrated PSF. They are background subtracted and dead time in burst option corrected. XIS2 was not used for this because it

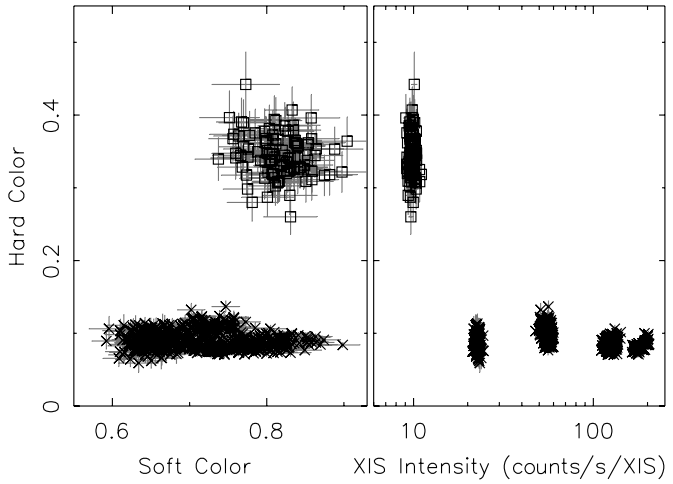

Figure 2. Color–color and hardness–intensity diagrams of 4U 1705–44 based on *Suzaku* observations in 2006–2008, with bin size 128 s. The squares are from observation 401046010 and the crosses from the other observations. For the definitions of the soft and hard colors, see the text. 1σ statistical error bars are also shown.

was not on for all observations. The count rates in the energy band 11.0–20.0 keV were from the PIN with the background subtracted and the dead time correction made. The CD and HID in Figure 2 use the 128 s data. The intensity is from the energy band 2.2–8.6 keV. Two type-I X-ray bursts were found in observation 401046010, and data around them are not included in Figure 2 or our spectral analysis. The data points with hard color larger than 0.2 (square symbols) are all from observation 401046010, indicating that only this observation was in the hard state while all other observations (cross symbols) were in the soft state.

Most observations show little variation (the average and standard deviation of colors are given in Table 1), and we created one spectrum each observation for spectral modeling. Each spectrum has three instrumental components, i.e., XIS023 (combination of XIS0, 2, and 3), XIS1, and PIN. In the end, we have seven spectra from *Suzaku* observations and they are denoted as *suz*1–*suz*7 hereafter (Table 1). We rebinned the spectra by factors of 8 and 16 for energies below and above 2.55 keV, respectively, and further rebinning was made so that every bin has at least 40 counts and χ^2 minimization criterion can be used in our spectral fitting.

2.2. *BeppoSAX* Data

There are two pointed observations of 4U 1705-44 with *BeppoSAX*, one on 2000 August 20 in the soft state and the other on 2000 October 3 in the hard state (Table 2; Fiocchi et al. 2007). The publicly available data are from three narrow field instruments: the Low Energy Concentrator Spectrometer (LECS, 0.1–10 keV; Parmar et al. 1997), the Medium Energy Concentrator Spectrometer (MECS, 1.3–10 keV; Boella et al. 1997), and the Phoswich Detection System (PDS, 15–300 keV; Frontera et al. 1997). There are three MECS units (MECS1, 2, 3), but no data from MECS1 are available during these two observations. Thus we used only data from MECS2 and 3. We extracted two spectra, one for the soft-state observation and the other for the hard-state observation, and they are denoted as *sax*1 and *sax*2 hereafter (Table 2). The LECS and MECS data were extracted from circular regions of 8′ radius centered on the source position. As our source is in the direction of the Galactic ridge, we cannot use "blank fields" measurement for background

Table 2
BeppoSAX Observations of 4U 1705–44

Observation ID	21292001	21292002
Spectral ID	*sax*1	*sax*2
Observations		
Observation date	2000 Aug 20	2000 Oct 03
Exposure of LECS/MECS/PDS (ks)	20.6/43.5/20.2	14.8/46.8/20.7
MECS2 count rate (counts s^{-1})	27.9	4.5
Spectral state	Soft	Hard

subtraction for the LECS. Instead, we used the semi-annuli method described in Parmar et al. (1999). For the MECS, we used the "blank fields" method for the MECS as described in the instrument analysis guide. The PDS spectra were also extracted, with the background rejection method based on fixed Rise Time thresholds. The background for the PDS spectra was obtained using observations during off-source intervals. All the spectra for each instrument were finally rebinned using the publicly available template files to sample the instrument resolution with the same number of channels at all energies.

3. SPECTRAL MODELING

3.1. Spectral Models and Assumptions

We fit all nine spectra, *suz*1–*suz*7 from *Suzaku* and *sax*1–*sax*2 from *BeppoSAX*. For *Suzaku*, we jointly fit spectra from XIS023, XIS1, and the PIN. We used the energy bands with good calibration and high signal-to-noise ratios for each instrument: 1.2–1.7, 1.9–2.2, and 2.3–10 keV for XIS detectors, and 11.0–40.0 keV for the PIN. Their relative normalizations were left free, and the spectral fit results quoted later are all from XIS023 (results from XIS1 differ by <3% generally). For *BeppoSAX* spectra, we jointly fit the LECS, MECS2, MECS3, and PDS. We utilized the 1.0–3.5 keV energy band for the LECS, 1.7–10.0 keV for the MECS, and 15.0–40.0 keV for the PDS (15.0–150.0 keV for the hard-state spectrum *sax*2). Their relative normalizations are also left free, but that of PDS relative to MECS was constrained to the range 0.77–0.93, a 90% confidence interval advised by the instrument analysis guide. The spectral fit results quoted later are all referenced to MECS2 (results from MECS3 differ by <2%). The fit of the Crab Nebula from the MECS using a single power law gives the photon index 2.1 and normalization 9.23, while the XIS gives 2.1 and 9.55, respectively. Thus the normalizations from both observatories appear to differ by less than 5%. For all spectral fits, we set the model systematic error to be 1%.

For the soft-state spectra, we tested three models for the continuum spectra: MCD+BB, MCD+BB+PL, and, SIMPL(MCD)+BB, respectively, where PL is a power law and SIMPL is a simple-Comptonization model by Steiner et al. (2009). MCD (diskbb in XSPEC) has two parameters: the temperature $kT_{\rm MCD}$ at the apparent inner disk radius $R_{\rm MCD}$, and the other is the normalization $N_{\rm MCD} \equiv (R_{\rm MCD,km}/D_{10\,\rm kpc})^2 \cos i$, where $D_{10\,\rm kpc}$ is the distance to the source in unit of 10 kpc and i is the disk inclination. BB (bbodyrad in XSPEC) assumes an isotropic BB spherical surface with radius $R_{\rm BB}$ and has two parameters, i.e., the temperature $kT_{\rm BB}$ and the normalization $N_{\rm BB} \equiv (R_{\rm BB,km}/D_{10\,\rm kpc})^2$. SIMPL (in XSPEC12) is an empirical convolution model of Comptonization in which a fraction of the photons from an input seed spectrum is scattered into a power-law component. This model has only two free parameters, i.e., the photon power-law index $\Gamma_{\rm SIMPL}$ and the scattered

fraction f_{SC}. In addition, there is a flag parameter to control whether all the scattered photons are up-scattered in energy or are both up- and down-scattered. We specified that all the scattered photons are up-scattered in energy. We found that inclusion of down-scattering only changed our results within error bars. We assumed that the Comptonization seed photons are from the disk. The fit results of the MCD and BB are consistent within error bars if we assumed both the MCD and BB contribute to the Comptonization seed photons instead, thanks to low Comptonization for all our soft-state observations. The best-fitting photon power-law index Γ_{SIMPL} turns out to be high (>4) in most cases, a regime where the model is not suitable (Steiner et al. 2009). Thus, we constrained Γ_{SIMPL} to be less than 2.5, a value typically seen in the black hole cases. No constraint on the photon index Γ_{PL} in the PL model was used.

The two hard-state continuum spectra *sax*2 and *suz*1 were fit with a BB plus a Comptonized component. We tested three choices of the Comptonization component: a broken power law (BPL; bknpower in XSPEC), a cutoff power law (CPL; cutoffpl in XSPEC), and the Comptonization model by Titarchuk (1994; CompTT in XSPEC). CompTT is an analytic model describing Comptonization of soft photons in a hot plasma.

All models included an absorption component (we use model wabs in XSPEC). There are strong broad Fe lines in most spectra (see also Reis et al. 2009). They were modeled by the diskline model (Fabian et al. 1989), which describes line emission from a relativistic accretion disk. Its parameters are: the line energy E_{line} in unit of keV, the power law dependence of emissivity (β), the disk inner and outer radii in units of GM/c^2, the disk inclination i, and the normalization (photons cm^{-2} s^{-1}). Figure 3 shows some examples of unfolded spectra at different states using different models, with the Fe lines modeled by the diskline model. The top panel shows the hard-state spectrum *sax*2 using model CPL+BB. The lower two panels show the soft-state spectrum *suz*2 using models MCD+BB+PL and SIMPL(MCD)+BB, respectively.

We scaled the luminosity and radius related quantities using a distance of 7.4 kpc (Haberl & Titarchuk 1995), unless indicated otherwise. The flux and its error bars are all calculated for an energy band of 0.001–200 keV (1.5–200 keV for CPL/PL components) using the cflux model in XSPEC12. As there is little emission of the thermal components outside the above energy band, the values are essentially bolometric for thermal components. For the MCD component, we assume the inclination to be 24°, from the fitting of Fe lines (see below).

3.2. Spectral Fit of the Soft-state Spectra and Results

We test three models for the soft-state continuum spectra: MCD+BB, MCD+BB+PL, and SIMPL(MCD)+BB. Our practice is to use a fixed value of the interstellar column density (N_H) for all spectral fits of each model. To determine for the appropriate value, we fit all soft-state spectra (*suz*2 − *suz*7 and *sax*1) simultaneously with each model, while tying their N_H to a common value. The best-fitting values of N_H for MCD+BB, MCD+BB+PL, and SIMPL(MCD)+BB are (1.69 ± 0.01), (1.88 ± 0.06), and $(1.71 \pm 0.01) \times 10^{22}$ cm^{-2}, respectively. The above values are obtained from fits with the Fe line region 4.0–8.0 keV excluded, although the fits with the Fe line modeled by the diskline model give very similar values. We see that models MCD+BB and SIMPL(MCD)+BB yield similar values of N_H, but they are smaller than that from model MCD+BB+PL. This is consistent with the results of Steiner et al. (2009), i.e., fits with PL tend to infer higher values of N_H than fits with SIMPL, a systematic effect of different ways of handling the Comptonization. Considering this issue, we do not require a common value of N_H for all models, but use $N_H = 1.71 \times 10^{22}$ cm^{-2} for models MCD+BB and SIMPL(MCD)+BB, and 1.88×10^{22} cm^{-2} for model MCD+BB+PL. In the latter case, the choice of either value of N_H does not affect the spectral parameters for the MCD and BB components very much, but there are obvious differences for the PL component, as will be discussed below.

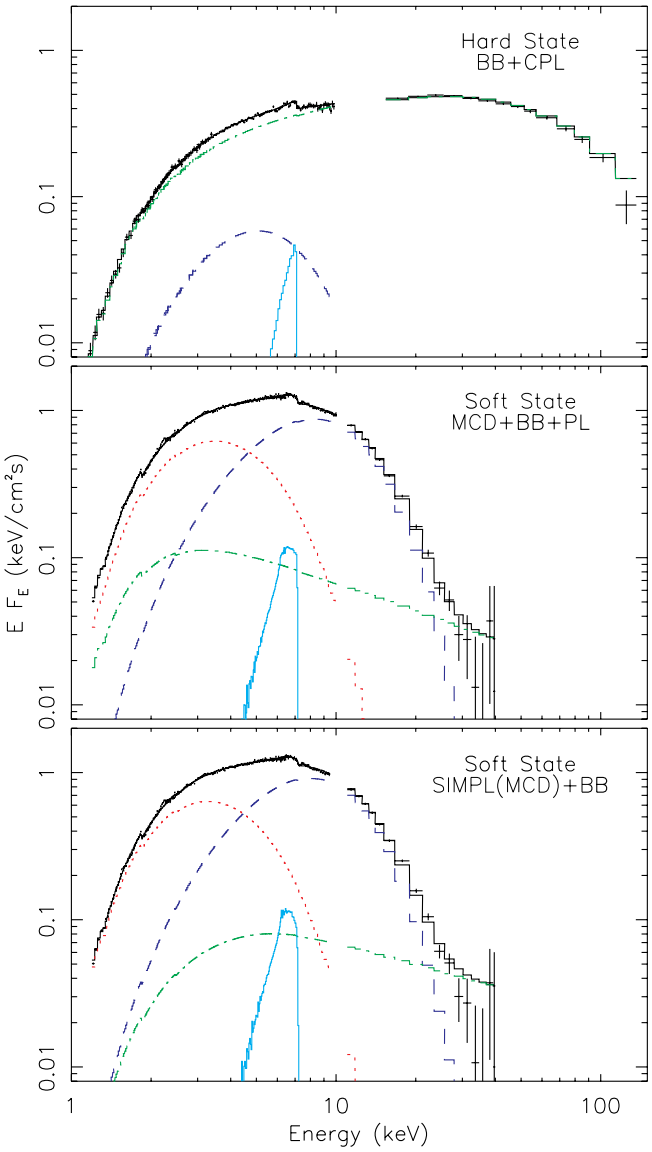

Figure 3. Examples of unfolded spectra from different states using different models. The total model fit is shown as a black solid line. The MCD component (if included) is shown by a red dotted line, the BB component by a blue dashed line, the PL/CPL/SIMPL component by a green dot-dashed line, and the Fe line (modeled by the diskline model) by a cyan triple-dot-dashed line. For the SIMPL(MCD)+BB model, the MCD component shown is the unscattered part, and the plotted SIMPL component refers to the scattered part. The hard-state spectrum is from *sax*2, and the soft-state spectrum from *suz*2.

(A color version of this figure is available in the online journal.)

The spectral fit results of the thermal components (MCD and BB) in the soft state from all tested models with the Fe line included are shown in Figure 4, and results of all spectral components are tabulated in Tables 3 (MCD+BB+PL+diskline) and 4 (SIMPL(MCD)+BB+diskline). The details of fitting the Fe line with the diskline model are given in Section 3.4.

The red crosses and the black triangles in Figure 4 are for soft-state spectra *suz*2–*suz*7 and *sax*1, respectively, and the panels from the top to the bottom correspond to continuum models MCD+BB, MCD+BB+PL, and SIMPL(MCD)+BB, respectively. For model SIMPL(MCD)+BB, the MCD component shown is the original value before scattering. The dotted lines in Figure 4 correspond to the NS burst radius of $R_{\rm burst} \sim 7.4$ km (at a distance of 7.4 kpc), assuming $L_{\rm X} = 4\pi R^2 \sigma T^4$. The NS radius was derived from spectral fitting to Type I X-ray bursts of this source using *RXTE* data (see also Gottwald et al. 1989). The dashed lines correspond to $R = 2.2$ km, which is about the average visible BB emission size.

From Figure 4, we see that the MCD and BB components in the soft state roughly follow the $L \propto T^4$ tracks for all models, which implies relatively constant apparent emission areas. We discuss the extent of deviation in Section 4. The inner disk radius is comparable with the NS radius, while the visible BB emission area is about 1/11 of the NS surface. The $kT_{\rm MCD}$ has values from ~0.8 to 1.7 keV, and $kT_{\rm BB}$ from ~1.8 to 2.4 keV. These values are roughly similar to those seen in Aql X-1, 4U 1608-52, and XTE J1701-462 in the atoll soft state (Lin et al. 2007, 2009). Fits with the Fe line region excluded from the fit generally give consistent results for the MCD and BB components, to within 10% for the normalization parameter $N_{\rm MCD}$ and within 20% for the $N_{\rm BB}$. Spectrum *sax*1 gives larger differences (~40% for $N_{\rm BB}$), probably because of its narrower energy band and lower energy resolution (only five channels above 10 keV and none in the energy band of 10–15 keV).

Results of the thermal components from both models MCD+BB+PL and SIMPL(MCD)+BB are generally similar, but differences of >20% can occur in some cases (e.g., 30% for $N_{\rm MCD}$ from the spectrum *suz*2; compare Tables 3 and 4). Due to weak Comptonization in the soft state, model MCD+BB in general also gives similar results of the thermal components (e.g., flux differs <5% and $N_{\rm BB}$ by <20%) and acceptable reduced χ^2 values (<2.0; but 2.6 for *sax*1). The largest differences in best-fitting spectral parameters from model MCD+BB compared with those from models MCD+BB+PL and SIMPL(MCD)+BB are from *BeppoSAX* spectrum *sax*1 ($N_{\rm BB}$ differs by ~50%).

3.3. Spectral Fit of the Hard-state Spectra and Results

We first investigate the performance of different Comptonization models. Using spectrum *sax*2, which extends to 150 keV (instead of 40 keV for spectrum *suz*1), we obtained values of χ^2/ν 190.2/226, 287.1/224, and 339.9/225 for models CPL+BB, BPL+BB, and CompTT+BB, respectively ($N_{\rm H}$ was allowed to have different values for different models). The result for CompTT+BB quoted above is just one possible solution with a local χ^2 minimum. The best-fitting input seed photon temperature τ_0 is <0.2 keV (the cold seed photon model; Lin et al. 2007). All the above models give similar results in terms of $kT_{\rm BB}$ (~1.5 keV), $N_{\rm BB}$ ($\lesssim$20), and the Comptonization fractions (>90%). There is another solution for CompTT+BB, which has $\chi^2/\nu = 252.5/225$. It has $\tau_0 = 0.9 \pm 0.1$ keV (the hot seed photon model; Lin et al. 2007). For this case, the inferred BB component is quite different from the models above, with $kT_{\rm BB} = 0.5 \pm 0.1$ keV and $N_{\rm BB} = 256 \pm 110$. The fit residuals of all the above models are shown in Figure 5. We see that CPL+BB gives the best fit over the whole energy range, while other models tend to have large residuals at high energy (>15 keV). Hereafter, we focus on model CPL+BB only.

The fit of the CPL model to the *BeppoSAX* hard-state 15.0–150.0 keV spectrum (the BB contributes little at energies above 15.0 keV) gives a cutoff energy of 44 ± 4 keV. The cutoff energy cannot be well constrained in the case of spectrum *suz*1, for which we use energies only up to 40 keV. Thus, we fixed the cutoff energy to be 44 keV when we fit spectra *sax*2 and *suz*1. The simultaneous fit of *sax*2 and *suz*1 gives a best-fitting value

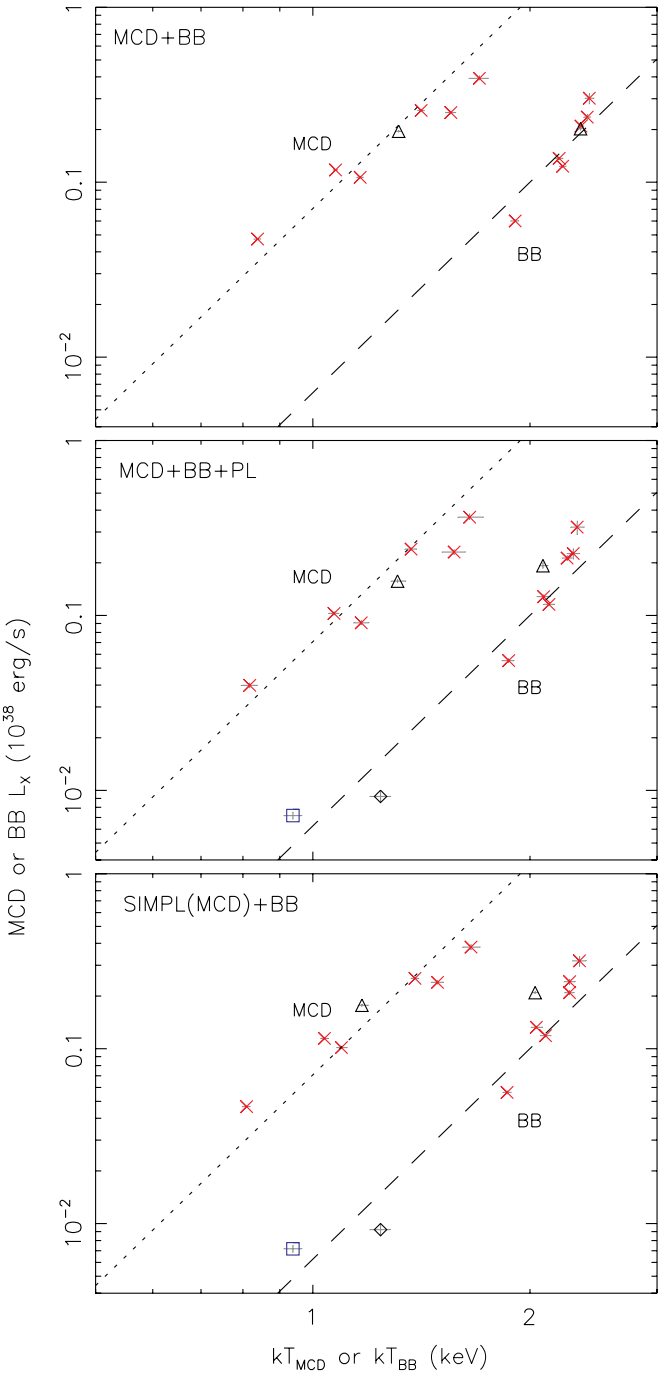

Figure 4. Luminosity of the thermal components versus their characteristic temperatures. Each model includes the diskline component to fit the Fe line. The symbols in each panel denote different spectral states and different observatories: *BeppoSAX* hard (black diamond) and soft (black triangle) states, and *Suzaku* hard (blue square) and soft (red crosses) states. For the case of Model SIMPL(MCD)+BB, the MCD component shows the original seed spectrum luminosity (i.e., before scattering). The dotted lines correspond to the NS burst radius of 7.4 km (see the text), and the dashed lines correspond to $R_{\rm BB} = 2.2$ km. Error bars at a 90% confidence level are also shown, but mostly are smaller than the symbol size.

(A color version of this figure is available in the online journal.)

Table 3
Spectral Modeling Results of Soft-state Observations Using MCD+BB+PL+Diskline

Spectral ID	$kT_{\rm MCD}$ (keV)	$N_{\rm MCD}$	$kT_{\rm BB}$ (keV)	$N_{\rm BB}$	$\Gamma_{\rm PL}$	$N_{\rm PL}$	$E_{\rm line}$ (keV)	β	EW (eV)	$\chi^2_\nu(\nu)$	$L_{\rm X,Edd}$
*suz*3	0.82 ± 0.02	114 ± 13	1.87 ± 0.03	6.43 ± 0.53	2.71 ± 0.08	0.17 ± 0.02	$6.87_{-0.12}$	−4.55 ± 0.50	160 ± 24	1.27(703)	0.044 ± 0.001
*suz*6	1.07 ± 0.02	101 ± 6	2.12 ± 0.04	8.05 ± 0.57	2.77 ± 0.07	0.33 ± 0.02	$6.92_{-0.08}$	$-4.06^{+0.35}_{-0.54}$	176^{+11}_{-29}	1.05(708)	0.098 ± 0.002
*suz*2	1.17 ± 0.03	63 ± 4	2.09 ± 0.04	9.53 ± 0.91	2.65 ± 0.07	0.30 ± 0.02	$6.94_{-0.05}$	−3.64 ± 0.27	160 ± 20	1.04(708)	0.099 ± 0.002
*sax*1	1.31 ± 0.03	68 ± 5	$2.08^{+0.03}_{-0.02}$	$14.46^{+0.83}_{-1.19}$	$2.69^{+0.02}_{-0.04}$	0.62 ± 0.03	$6.97_{-0.05}$	−3.59 ± 0.20	156^{+41}_{-9}	1.08(217)	0.163 ± 0.003
*suz*5	1.37 ± 0.02	88 ± 5	2.25 ± 0.03	11.73 ± 0.89	2.72 ± 0.09	0.38 ± 0.04	$6.95_{-0.06}$	−3.45 ± 0.28	154^{+36}_{-20}	1.00(706)	0.192 ± 0.004
*suz*7	1.57 ± 0.06	48 ± 5	2.3 ± 0.04	11.5 ± 1.47	2.67 ± 0.08	0.44 ± 0.04	$6.89_{-0.08}$	$-3.38^{+0.28}_{-0.46}$	165 ± 26	0.99(706)	0.198 ± 0.007
*suz*4	1.65 ± 0.07	61^{+9}_{-6}	2.33 ± 0.05	15.51 ± 2.48	$2.77^{+0.16}_{-0.11}$	0.50 ± 0.06	$6.97_{-0.05}$	−3.4 ± 0.30	118^{+35}_{-17}	1.00(702)	0.285 ± 0.012

Notes. They are listed in order of the source total luminosity. See Section 3.1 for the meaning of each parameter. The normalizations of the MCD and BB models are based on the assumption that the distance to the source is 10 kpc. For the diskline model, the inclination is fixed at 24°, and inner disk radius at $6\,GM/c^2$ (see the text). EW is the equivalent width of the Fe line modeled by the diskline model, but it is not a parameter of the model. The last column is the total luminosity in units of the Eddington luminosity (Section 3.2), and the error bars are calculated based on simple error propagation from individual spectral components.

Table 4
Spectral Modeling Results of Soft-state Observations Using SIMPL(MCD)+BB+Diskline

Spectral ID	$kT_{\rm MCD}$ (keV)	$N_{\rm MCD}$	$kT_{\rm BB}$ (keV)	$N_{\rm BB}$	$\Gamma_{\rm SIMPL}$	$f_{\rm SC}$	$E_{\rm line}$ (keV)	β	EW (eV)	$\chi^2_\nu(\nu)$	$L_{\rm X,Edd}$
*suz*3	0.81 ± 0.01	139 ± 6	1.86 ± 0.02	6.67 ± 0.37	$2.5_{-0.15}$	0.06 ± 0.02	$6.86_{-0.12}$	$-4.57^{+0.4}_{-0.59}$	163 ± 23	1.28(703)	0.044 ± 0.001
*suz*6	1.04 ± 0.01	127 ± 4	2.10 ± 0.03	8.63 ± 0.59	$2.5_{-0.16}$	0.04 ± 0.01	$6.95_{-0.09}$	−4.28 ± 0.43	173 ± 21	1.06(708)	0.097 ± 0.002
*suz*2	1.10 ± 0.02	90 ± 4	2.04 ± 0.04	10.82 ± 0.81	$2.5_{-0.15}$	$0.06^{+0.01}_{-0.02}$	$6.95_{-0.06}$	−3.79 ± 0.25	165 ± 20	1.05(708)	0.100 ± 0.002
*sax*1	$1.17^{+0.02}_{-0.01}$	121^{+3}_{-6}	2.03 ± 0.02	$17.16^{+1.02}_{-0.62}$	$2.5_{-0.1}$	0.05 ± 0.01	$6.97_{-0.03}$	−3.87 ± 0.19	187^{+32}_{-15}	1.31(217)	0.165 ± 0.002
*suz*5	1.39 ± 0.02	88 ± 3	2.27 ± 0.03	11.19 ± 0.77	$2.5_{-0.89}$	0.02 ± 0.01	$6.93_{-0.06}$	$-3.30^{+0.23}_{-0.34}$	161 ± 29	1.02(706)	0.185 ± 0.004
*suz*7	1.49 ± 0.03	62 ± 3	2.27 ± 0.04	12.90 ± 1.18	$2.5_{-0.45}$	0.03 ± 0.01	$6.9_{-0.06}$	$-3.48^{+0.25}_{-0.42}$	169^{+34}_{-21}	0.99(706)	0.197 ± 0.005
*suz*4	1.66 ± 0.05	65 ± 5	2.34 ± 0.05	14.94 ± 2.06	$2.11_{-0.61}$	0.01 ± 0.01	$6.97_{-0.05}$	−3.37 ± 0.28	117^{+34}_{-15}	1.00(702)	0.277 ± 0.010

Note. Same as Table 3, but for model SIMPL(MCD)+BB+diskline.

of $N_{\rm H} = (1.89 \pm 0.04) \times 10^{22}$ cm^{-2} from model CPL+BB, close to the value of 1.88×10^{22} cm^{-2} obtained from model MCD+BB+PL for the soft state. For comparison, we fit the hard-state spectra using both $N_{\rm H} = 1.88$ and 1.71×10^{22} cm^{-2}, and the results are given in Table 5. We see no large different between these two sets of solutions. Using $N_{\rm H} = 1.88 \times 10^{22}$ cm^{-2} tends to give a smaller BB emission area and a higher photon index of the CPL model. The values of the photon index are more similar between spectra *sax*2 and *suz*1 than using $N_{\rm H} = 1.71 \times 10^{22}$ cm^{-2}. Both values of $N_{\rm H}$ give high fractions of Comptonization (>90%).

The results using $N_{\rm H} = 1.88 \times 10^{22}$ cm^{-2} are shown in Figure 4, the blue squares and the black diamonds for *suz*1 and *sax*2, respectively. They are repeated in the middle and bottom panels. They are not shown in the top panel, because this panel is reserved for solutions free of Comptonization and such a model is unacceptable for observations of the hard state. From Figure 4, we see that the boundary layer emission areas in the hard state are comparable to those in the soft state. Although $L_{\rm BB}$ changes over 50 times, the values of $N_{\rm BB}$ are always in the range of ∼5–15.

One of our main goals of using the broadband spectra is to search for detectable thermal emission from the accretion disk in the hard state. We added the MCD component while analyzing the two hard-state spectra (*suz*1 and *sax*2), i.e., using model CPL+MCD+BB, with either the Fe modeled with the diskline model or with the Fe region excluded in the fit. $N_{\rm H}$ is either fixed at 1.71 or 1.88×10^{22} cm^{-2}, or left free in the fit. The best-fitting disk temperature tends to go below 0.2 keV, with an upper limit <0.25 at a 90% confidence level. The normalizations of the MCD component $N_{\rm MCD}$ are not well constrained. For all cases, the unscattered flux of the MCD component is <2% of the total flux (absorbed or unabsorbed; 1–200 keV). Thus, if we assume a physically visible disk, then we cannot exclude either possibility, i.e., the disk in the hard state might be truncated at a very large radius and/or the temperature is below 0.2 keV. Alternatively, the disk may be rendered invisible by very high Comptonization.

Figure 6 shows the fraction of Comptonized luminosity versus the total luminosity, using SIMPL(MCD)+BB for the soft state and CPL+BB for the hard state. The total luminosity is normalized by the Eddington luminosity $L_{\rm Edd}$, which is derived from the type I X-ray bursts showing photospheric radial expansion and corresponds to an average peak flux of about 4×10^{-8} erg cm^{-2} s^{-1} (Galloway et al. 2006). Figure 6 shows that Comptonization only constitutes < 15% of the emission in the soft state, but >90% in the hard state. For the soft-state data, the fractional contribution of Comptonized luminosity decreases with luminosity on the whole, which is consistent with the behavior of atoll-type transients (Lin et al. 2007). The MCD+BB+PL model also gives low-Comptonization solutions for the soft state (<15%), with $N_{\rm H}$ either 1.71 or 1.88×10^{22} cm^{-2}. One main difference between these two choices of $N_{\rm H}$ is that fits with $N_{\rm H} = 1.88 \times 10^{22}$ cm^{-2} give higher values of $\Gamma_{\rm PL}$ (∼2.7) than fits with $N_{\rm H} = 1.71 \times 10^{22}$ cm^{-2} ($\Gamma_{\rm PL}$∼2.2).

The BB component, which describes the emission from the boundary layer in our model, is present in both the hard and soft

Table 5
Spectral Modeling Results of Hard-state Observations Using BB+CPL+Diskline

Spectral ID	N_H (10^{22} cm^{-2})	T_{BB} (keV)	N_{BB}	Γ_{CPL}	N_{CPL}	E_{line} (keV)	β	EW (eV)	$\chi^2_\nu(\nu)$	$L_{X,Edd}$
*suz*1	1.71f	0.94 ± 0.02	17.62 ± 1.58	1.19 ± 0.02	0.056 ± 0.002	6.60 ± 0.04	−2.45 ± 0.28	92 ± 27	1.10(676)	0.055 ± 0.001
*sax*2	1.71f	1.30 ± 0.03	6.06 ± 0.61	1.37 ± 0.01	0.119 ± 0.003	$6.80_{-0.13}$	−2.46 ± 0.55	93 ± 36	1.19(228)	0.070 ± 0.001
*suz*1	1.88f	0.94 ± 0.03	13.12 ± 1.62	1.33 ± 0.01	0.076 ± 0.002	6.59 ± 0.04	−2.30 ± 0.33	74 ± 28	1.06(676)	0.049 ± 0.001
*sax*2	1.88f	1.24 ± 0.04	5.52 ± 0.77	1.40 ± 0.01	0.135 ± 0.003	$6.87_{-0.15}$	−2.86 ± 0.55	126 ± 37	0.93(228)	0.070 ± 0.001

Notes. Same as Table 3, but for model BB+CPL+diskline and for the hard-state data. The cutoff energy of the CPL is fixed at 44 keV.

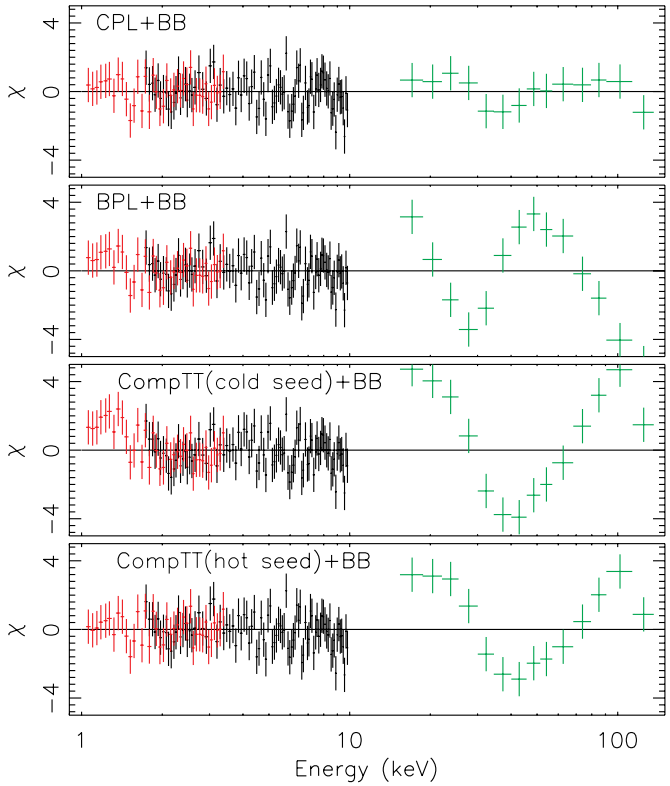

Figure 5. Fit residuals in terms of sigmas with error bar values set to be one for different Comptonization models in combination with BB model, using the hard-state spectrum *sax*2. The red, black, green points are from LECS, MECS2, and PDS, respectively.

(A color version of this figure is available in the online journal.)

states. We can compare this component with the other spectral components to investigate the impact of different accretion processes in different states. We plot in Figure 7 the luminosity of the MCD component plus Comptonization (SIMPL/CPL) versus the BB luminosity from model SIMPL(MCD)+BB. Model MCD+BB+PL gives similar results. The hard-state data (diamond and square symbols) are from model CPL+BB. The dashed and dotted lines correspond to the ratios of 1 and 0.05 of the BB luminosity versus the MCD component plus Comptonization luminosity, respectively. They are about the average values for the soft- and hard-state observations, respectively. If we assume that the Comptonization emission is not from the boundary layer, the above result means that there is a much lower portion of energy seen in the visible portion of the boundary layer in the hard state than in the soft state. Similar results were suggested to be a possible consequence of a strong jet in the hard state in Lin et al. (2007).

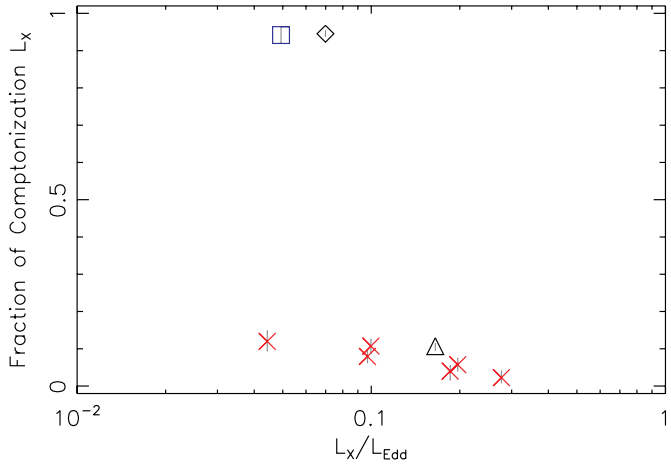

Figure 6. Energy fraction of Comptonized luminosity vs. the total luminosity, from model SIMPL(MCD)+BB (the soft state) and model CPL+BB (the hard state). See Figure 4 for meanings of symbols. Error bars at a 90% confidence level are shown for the fraction of Comptonization Lx, and those for Lx/LEdd are not shown, but all are very small (Tables 3–5).

(A color version of this figure is available in the online journal.)

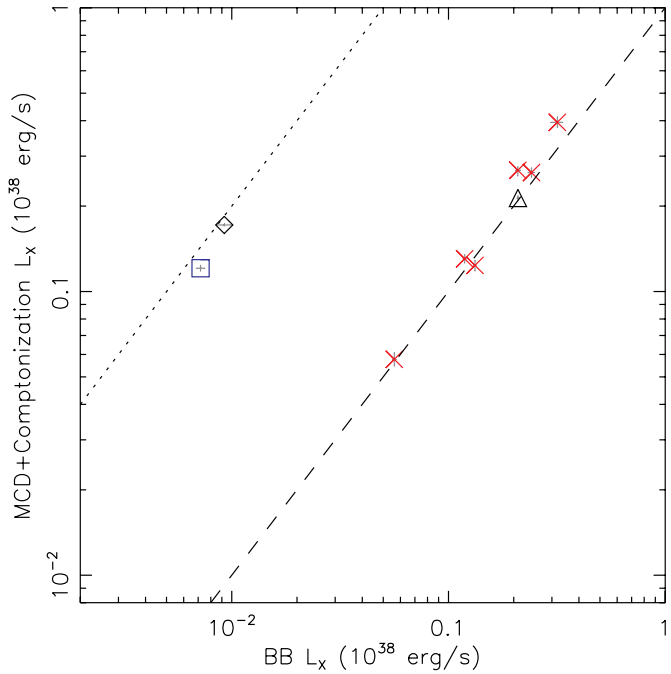

Figure 7. Luminosity of the MCD component plus Comptonization vs. the BB luminosity. The results for the soft state are from model SIMPL(MCD)+BB+diskline, and the Comptonization refers to the scattered disk emission, modeled by SIMPL. Model MCD+BB+PL+diskline gives similar results. The dashed and dotted lines mark the ratios of 1 and 0.05 of the BB luminosity versus the MCD component plus Comptonization luminosity, respectively. See Figure 4 for meanings of symbols. Error bars at a 90% confidence level are also shown, but mostly are smaller than the symbol size.

(A color version of this figure is available in the online journal.)

3.4. Relativistic Fe Lines

We first fit the Fe line with a Gaussian line. A broad Gaussian line with the line width σ around 0.6 is generally required, while fits with a narrow line ($\sigma < 0.1$ keV) are mostly unacceptable, with χ^2 values increased by >100 for ~700 degrees of freedom in the soft state. The diskline model can in general improve the fits further, compared with a broad Gaussian line, with the χ^2 values decreased by about 30 on average in the soft state. In the hard state, the diskline model still gives the best fits, though the improvement is much less. We also fit the spectra with a smeared edge (smedge in XSPEC) in our continuum model, with the lower limit of the threshold energy set to be the neutral Fe K edge 7.1 keV. We obtain fits with χ^2 values larger than those using the diskline model by about 30 on average, and the threshold energy in most fits reaches the lower limit 7.1 keV. Thus the broad line feature in the spectra is probably not completely due to the Fe absorption edge. The more complicated model combining both a Gaussian line and a smeared edge can give fits with similar χ^2 values as those using the diskline model, but we choose to focus on the results using the simpler model, i.e., the diskline model.

While fitting the Fe line with the diskline models, we initially fit all soft-state spectra simultaneously, with the inclination parameter i tied to a common value. Different continuum models turn out to give quite similar best-fitting values of i: $24.^\circ3 \pm 0.^\circ8$, $23.^\circ3 \pm 1.^\circ0$, and $24.^\circ2 \pm 0.^\circ8$ from models MCD+BB, MCD+BB+PL, and SIMPL(MCD)+BB, respectively. Thus we fix the disk inclination to be $i = 24^\circ$. For most of the soft-state spectra, the inner disk radius inferred from the diskline model reaches 6 GM/c^2, the innermost stable circular orbit (ISCO). Thus in the final fitting, we fix it to be 6 GM/c^2. For the hard-state spectra, the Fe lines are much weaker, and the best-fitting inner disk radius in the diskline model is quite uncertain. The lower error bar reaches 6 GM/c^2 for the two observatories using both $N_{\rm H} = 1.88$ and 1.71×10^{22} cm^{-2}. For simplicity, we then fixed the inner disk radius in the diskline model to be 6 GM/c^2 for the hard-state spectra to derive the final results. The obtained Fe line flux and equivalent width are not sensitive to such details.

The results of fitting Fe lines with the diskline model are shown in Figure 8. It can be seen that the Fe emission line is detected in all spectra, and most of them show a broad feature (see also Reis et al. 2009). Tables 3–5 contain best-fitting parameters of the Fe line for each spectrum, with the equivalent width also included. The best-fitting value of $E_{\rm line}$ reaches the allowed upper limit 6.97 keV in most cases. The equivalent width is around 170 eV for most of the soft-state spectra, and it is around 100 eV in the hard state. The power-law dependence of emissivity β is generally steeper in the soft state (~ -3.5) than in the hard state (~ -2.5). We note that our detection of these relativistic Fe lines, mostly in the soft state, cannot be due to the pile-up effect (Ng et al. 2010), as we have excluded enough pile-up regions when we extract the *Suzaku* spectra. Moreover, the *BeppoSAX* detectors have no pile-up problem, and its spectrum *sax1* also shows the relativistic feature.

Fe emission lines in X-ray binaries are the most obvious signature of an accretion disk irradiated by an external source of hard X-rays, due to a combination of high fluorescent yield and large cosmic abundance (Miller 2007). To investigate the irradiation source of the Fe lines, we show in Figure 9 the dependence of the bolometric Fe energy line flux on the BB energy flux (upper panel) and Comptonization (SIMPL/CPL) flux (lower panel), both integrated over 6.4–200 keV. The soft-state data show that the Fe line flux increases monotonically with the BB flux, but has no clear dependence on the Comptonization

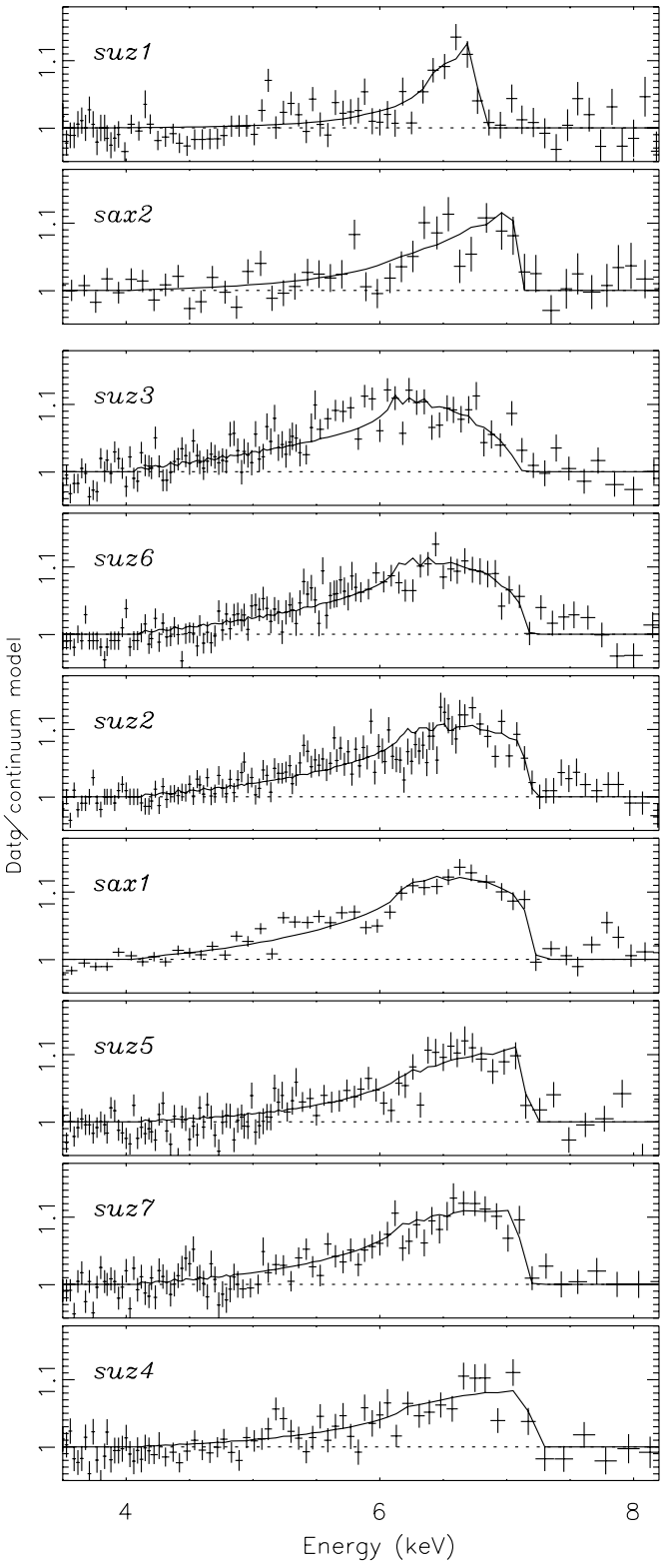

Figure 8. Fe lines of all spectra, fit by the diskline model. The upper two panels are for the hard state (spectra *suz*1 and *sax*2), while others for the soft state. The soft-state continuum is fit by model SIMPL(MCD)+BB, while model MCD+BB+PL gives very similar results. From top to bottom, the source luminosity increases, except for the hard-state spectra *suz*1 and *sax*2, which are put on the top panels and have luminosities between that of *suz*3 and *suz*6.

flux. This might imply that it is the boundary layer emission that illuminates the accretion disk and produces the Fe line, in agreement with the conclusions of Cackett et al. (2009a). The

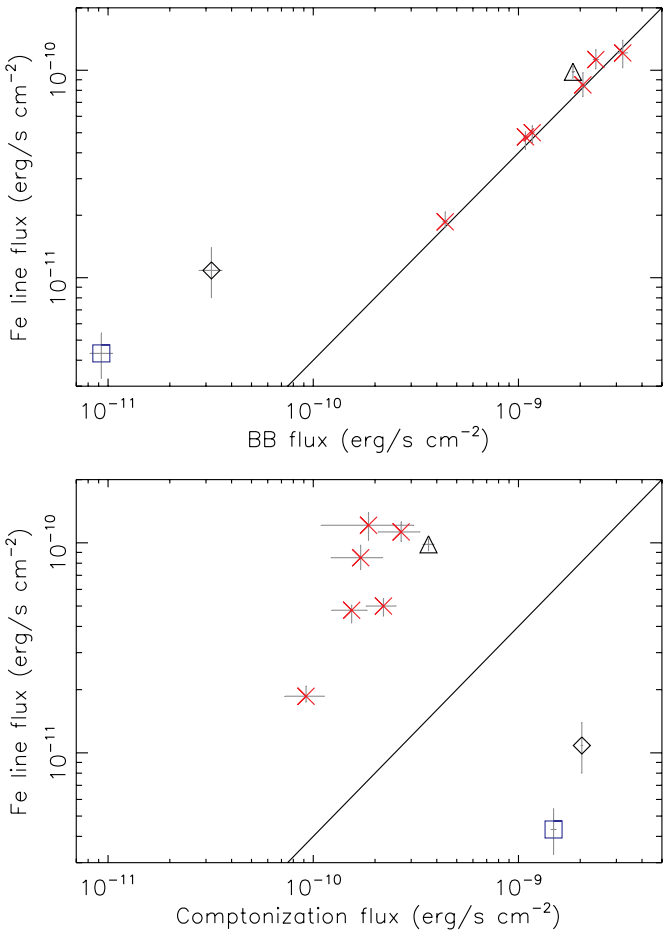

Figure 9. Dependence of Fe line flux on the BB flux (upper panel) and Comptonization flux (SIMPL/CPL components; lower panel). The solid lines mark the ratio of 4% of the Fe line flux over the BB flux or the Comptonization flux. The Fe line flux is bolometric, but the BB flux and Comptonization flux are integrated over 6.4–200 keV. See Figure 4 for meanings of symbols. Error bars at a 90% confidence level are also shown, but mostly are smaller than the symbol size.

(A color version of this figure is available in the online journal.)

Fe line energy flux is about 4% of the BB energy flux (solid lines).

The hard-state data in Figure 9 (diamond/square symbols) in the upper panel show that there is much higher Fe line flux relative to the BB continuum in the hard state compared to the soft state. This might indicate that the BB emission is not the (major) source illuminating the accretion disk to produce the Fe line in the hard state. From the lower panel, we can see that there is strong Comptonization flux available in the hard state. However, using the reference lines and comparing the upper and lower panels, we see that the Comptonization emission is not as efficient as the BB emission to illuminate the accretion disk and produce the Fe line. This can be explained if the Comptonization emission is located farther away from the accretion disk than the boundary layer. We also caution that some BB flux may be screened from the observer's view by the accretion disk.

4. DISCUSSION

4.1. Global View of Two Spectral States

We have shown that 4U 1705-44 exhibits two distinct spectral states. The hard-state spectra span from ∼1 to 150 keV, while the soft-state spectra are mostly confined below 40 keV (see also Fiocchi et al. 2007). Such two distinct states have been observed in other atoll-type NS LMXBs (Barret 2001; van der Klis 2006). On the whole, these two spectral states are very similar to the thermal and hard states (but not the steep power-law state) of accreting black holes (Remillard & McClintock 2006; Done et al. 2007). In addition, atoll-type NS LMXBs and accreting black holes also have many similarities in timing properties. All this motivates the speculation that the accretion process is quite similar between atoll-type NS LMXBs and accreting black holes (Barret 2001; Done et al. 2007; Lin et al. 2007). This implies that the presence of the boundary layer in atoll-type NS LMXBs probably does not strongly interfere with the accretion disk, at least at luminosities below ∼0.5 $L_{\rm Edd}$. However, the boundary layer is still an important spectral component in atoll-type NS LMXBs. Figure 7 shows that the boundary layer emission flux is comparable with that from the disk. Because the boundary layer is hotter than the disk (Mitsuda et al. 1984), the soft-state spectra tend to cover a broader energy band and extend to higher energies in atoll-type NS LMXBs than in the thermal state of accreting black holes (compare our Figure 3 and Figure 2 in Remillard & McClintock 2006). The relatively weak contribution of the boundary layer in the hard state, as shown in Figure 7, can be interpreted as the consequence of mass ejection in this state (Lin et al. 2007). This seems to be in alignment with the jet model for the hard state in accreting black holes (Fender 2006; Done et al. 2007).

4.2. Inner Disk Radius

In Lin et al. (2007), our spectral modeling of two atoll sources Aql X-1 and 4U 1608-52, using the MCD+BB model plus weak Comptonization showed the MCD behavior close to the $L_{\rm MCD} \propto T_{\rm MCD}^4$ track. In contrast, classical two-component models resulted in constant or slightly decreasing temperatures of the thermal component (MCD or BB) with increasing luminosity. We note, however, that in that study we used *RXTE* data and the MCD component in the low-luminosity soft state could not be well constrained. In this study, we used *Suzaku* and *BeppoSAX* spectra, which extend the energy range down to 1 keV, and the MCD components are well constrained for all soft-state spectra. As the result of the better low-energy coverage, we did not need to put additional constraints on the PL component, as was necessary in Lin et al. (2007). This motivates us to evaluate more quantitatively how closely the MCD component follows the $L_{\rm MCD} \propto T_{\rm MCD}^4$ track.

Our spectral modeling of broadband spectra of 4U 1705-44 shows a track that is flatter than the $L_{\rm MCD} \propto T_{\rm MCD}^4$ relation, with nearly an order of magnitude variation in luminosity. There is a slight decrease of $R_{\rm MCD}$ at higher luminosity. Spectral fitting with Comptonization modeled by PL suggests $L_{\rm MCD} \propto T_{\rm MCD}^{3.3\pm0.2}$, while fitting by SIMPL results in $L_{\rm MCD} \propto T_{\rm MCD}^{3.1\pm0.1}$. Such deviations have been seen in several black-hole X-ray binaries, and it is normally believed to be due to a spectral hardening effect, instead of a real change in the inner disk radius (Shafee et al. 2006; Davis et al. 2006; McClintock et al. 2007, 2009). Spectral hardening arises when the electron scattering dominates over absorption as the main opacity source. In such a situation, the local specific flux in the disk appears as a simple dilute BB with a color temperature higher than the effective temperature by a factor of $f_{\rm col}$ (Shimura & Takahara 1995). This factor slightly increases with luminosity/temperature. Based on a simple analytic estimate of the hardening factor, Davis et al. (2006) suggested a $L_{\rm MCD} \propto T_{\rm MCD}^3$ relation. It should be

noted that the extent to which the hardening factor depends on luminosity can vary with the inclination, the mass of the compact object, etc. A detailed numeric simulation to obtain how the hardening factor behaves for an accreting NS or direct accretion modeling to infer the real inner disk radius with more realistic spectral models incorporating many effects could provide further insights. We further note that there are possibly other factors causing the above deviation. We cannot exclude the possibility of real change of the inner disk radius in some part of the soft state. It is also possible that the above deviation is due to our simple descriptions of the weak Comptonization and the boundary layer.

4.3. Constraint on the Magnetic Field in 4U 1705–44

We perform a rough estimate of the magnetic field in 4U 1705-44, under the assumption that the disk is truncated at the ISCO in our soft-state observations. This requires the magnetic field to be dynamically unimportant for these soft-state observations. That is, the Alfvén radius $r_{\rm A}$, the radius at which the magnetic pressure is roughly the sum of the ram and gas pressure, should be smaller than the ISCO. Based on Equations (6.19–6.20) in Frank et al. (1985), we have

$$r_{\rm A} \sim 7.5 \left(\frac{k_{\rm A}}{0.5}\right) \left(\frac{M_{\rm NS}}{M_\odot}\right)^{1/7} \left(\frac{R_{\rm NS}}{10\ {\rm km}}\right)^{10/7} \times \left(\frac{L}{10^{37}\ {\rm erg\ s^{-1}}}\right)^{-2/7} \left(\frac{B}{10^8\ {\rm G}}\right)^{4/7} {\rm km}, \quad (1)$$

where B is the magnetic field strength at the surface of the NS and $k_{\rm A}$ is the correction from the spherical accretion to disk accretion and is about 0.5. This formula assumes a dipole magnetic field. We further assume $M_{\rm NS} = 1.4\ M_\odot$ (such that $R_{\rm in} = 12.4$ km), and $R_{\rm NS} = 10$ km. The above expression shows that the obtained value of B will only weakly depend on the NS mass (a power of 1/4). Using $L = 10^{37}$ erg s^{-1}, from the faintest soft-state spectrum *suz*3, and the constraint $r_{\rm A} < R_{\rm in}$, we find $B < 1.9 \times 10^8$ G. We can also assume that $r_{\rm A}$ is less than $R_{\rm NS}$, which would decrease the above limit by 30%.

4.4. The Boundary Layer

We see that the apparent emission of the boundary layer, modeled by BB, roughly follows $L_{\rm BB} \propto T_{\rm BB}^4$, from the hard to the soft states with the luminosity of the boundary layer covering ~0.003–0.12 $L_{\rm Edd}$. The apparent area of the boundary layer is about 1/11 of the the NS surface, as inferred from Type I X-ray bursts. The actual area of the boundary layer might be larger due to a special geometry of the boundary layer, which has been attributed to be an equatorial belt (Lin et al. 2007). Using Equation (3) in Lin et al. (2007) and using the inclination obtained from the Fe line fit ($i = 24°$), the latitude range (from the NS equator) of the boundary layer is about 13°, corresponding to an emission area of 23% of the NS surface. Accordingly $L_{\rm BB}$ should be 1.6 times larger than shown in Section 3, which assumes isotropic emission of the boundary layer. Thus, $L_{\rm BB}/L_{\rm MCD+Comptonization}$ is not around 1 in the soft state, as shown in Figure 7, but is about 2.6. If $i = 60°$, the latitude range of the boundary layer is about 7°, corresponding to an emission area of 12% of the NS surface. In this case, $L_{\rm BB}$ should be 30% larger than shown in Section 3. $L_{\rm MCD}$ should increase by 80% (i.e., adjusting for $i = 60°$) so that $L_{\rm BB}/L_{\rm MCD+Comptonization}$ would be around 0.7 in the soft state.

Whether the above results imply that the real boundary layer area is small and nearly constant further depends on the radiative transfer process in the atmosphere above the boundary layer, i.e., the hardening effect as discussed above for the disk spectra. The small BB emission area is reminiscent of the well known spectral modeling problem of the NS thermal emission in quiescence, i.e., the BB fit of its thermal component produced inferred radii too small for theoretical NS size estimate, whereas models taking into account the radiative transfer in the hydrogen atmosphere give radius estimate much closer to theoretical expectation of the size of NSs (e.g., Rutledge et al. 1999). However, all our observations are quite bright ($\gtrsim 10^{37}$ erg s^{-1}), and the emission should be due to active accretion. At such a high accretion rate, a pure hydrogen atmosphere is not expected (Brown et al. 1998), and the above problem might not apply to our case. Our conclusion of the small size of the boundary layer is based on the assumption that the modification of the bursting atmosphere on burst emergent spectra is similar to that of the boundary layer emission. This assumption might be valid if most of the heat in the boundary layer is generated in a layer as deep as that for burst nuclear burning. We note that the small inferred size of the boundary layer agrees with the theoretical expectation of most of the boundary layer models at sub-Eddington accretion rates (Kluzniak & Wilson 1991; Inogamov & Sunyaev 1999; Popham & Sunyaev 2001). Thus it is quite possible that the boundary layer emission area is indeed small for our observations.

If the behavior of the hardening factor for the boundary layer is similar to that for the burst emission, then one might conclude that the boundary layer emission area is constant if $L_{\rm BB} \propto T_{\rm BB}^4$ is measured, as the hardening factor is quite independent of the temperature for burst emission in sub-Eddington limit (Madej et al. 2004; Özel 2006). For example, for an NS with mass 1.4 $M_\odot$ and radius 10 km, Table 2 from Madej et al. (2004) suggests an approximate relation of $L_{\rm BB} \propto T_{\rm BB}^{3.7}$ for $T_{\rm BB}$ within 1.1–2.5 keV (most of our observations fall into this range). Thus, our results of roughly following $L_{\rm BB} \propto T_{\rm BB}^4$ from the hard to soft states might imply little change of the real boundary layer emission area for our observations.

We note that there is scatter in the inferred apparent emission area of the boundary layer. The fractional variation is about 40%, larger than the typical error bars (10%). There are also systematic differences in the inferred boundary layer emission area between *BeppoSAX* and *Suzaku*, both in the hard and soft states (see Tables 3–5). Whether all this is real or affected by systematic problems related to spectral models and/or instrumentation is unclear. If we do a simple power-law fit as we did for the MCD component, the BB component seems to follow $L_{\rm BB} \propto T_{\rm BB}^{5.0\pm0.2}$ from fit to all data combined and $L_{\rm BB} \propto T_{\rm BB}^{4.3\pm0.1}$ from fit to *Suzaku* data only. Because of the above uncertainties, we did not treat these deviations from $L_{\rm BB} \propto T_{\rm BB}^4$ as significant. A better understanding of our luminosity vs. temperature results for the disk and boundary layer of an accreting NS may be gained from further theoretical work on each component, and from additional observations, e.g., with improved statistics and dynamic range for samples of the hard state.

5. CONCLUSION

The broadband X-ray spectra of 4U 1705-44 obtained with *Suzaku* and *BeppoSAX* show two distinct hard and soft spectral states. These spectra have significantly better coverage in the

soft X-ray energy band compared with those from *RXTE*. We have successfully fit these spectra using a model similar to Lin et al. (2007).

The accretion disk in the soft state seems to approximately follow a $L \propto T^{3.2}$ track. One cause of the deviation from $L \propto T^4$ maybe a luminosity-dependent spectral hardening factor. However, it is still possible that the inner disk radius is really changing in some part of the soft state. We found no significant contribution of the thermal disk in our hard-state spectra above 1 keV, and the disk might be truncated at a large radius and/or has a low temperature (<0.2 keV), or is buried under high Comptonization. The boundary layer is roughly constant from the hard to soft states, with apparent emission size about 1/11 of the whole surface of the neutron star. Assuming that the disk is truncated by ISCO in the soft state or the NS surface, we estimated the magnetic field in 4U 1705-44 to be less than about 1.9×10^8 G.

Broad relativistic Fe lines are also detected in most of the spectra, especially in the soft state. We modeled them with the diskline model and found that the strength of the Fe line correlates well with the boundary layer emission in the soft state, with the Fe line flux about 4% of the flux from the boundary layer (>6.4 keV). In the hard state, our results suggest that the Fe lines are due to the strong Comptonization emission. However, the Comptonization emission in the hard state seems to illuminate the accretion disk and produce the Fe line not as efficiently as the boundary layer emission in the soft state, probably because the boundary layer is closer to the inner accretion disk.

The authors thank all members of the *Suzaku* team, especially Koji Mukai, for their support in the scheduling of observations and preparation of this paper. Support for this research was provided by the NASA Grant NNX08AC02G under the Suzaku guest observer program and the NASA contract to MIT for *RXTE* instruments.

REFERENCES

Barret, D. 2001, Adv. Space Res., 28, 307
Barret, D., & Olive, J.-F. 2002, ApJ, 576, 391
Barret, D., et al. 2000, ApJ, 533, 329
Boella, G., et al. 1997, A&AS, 122, 327
Boldt, E. 1987, Phys. Rep., 146, 215
Brown, E. F., Bildsten, L., & Rutledge, R. E. 1998, ApJ, 504, L95
Cackett, E. M., et al. 2008, ApJ, 674, 415
Cackett, E. M., et al. 2009a, arXiv:0908.1098
Cackett, E. M., et al. 2009b, ApJ, 690, 1847
Christian, D. J., & Swank, J. H. 1997, ApJS, 109, 177
Church, M. J., & Balucińska-Church, M. 2001, A&A, 369, 915
Davis, S. W., Done, C., & Blaes, O. M. 2006, ApJ, 647, 525
di Salvo, T., et al. 2009, MNRAS, 398, 2022
Di Salvo, T., Iaria, R., Burderi, L., & Robba, N. R. 2000, ApJ, 542, 1034
Di Salvo, T., et al. 2005, ApJ, 623, L121
Done, C., Gierliński, M., & Kubota, A. 2007, A&AR, 15, 1
Fabian, A. C., Rees, M. J., Stella, L., & White, N. E. 1989, MNRAS, 238, 729
Fender, R. 2006, in Compact Stellar X-ray Sources, ed. W. Lewin & M. van der Klis (Cambridge: Cambridge Univ. Press), 381
Fiocchi, M., Bazzano, A., Ubertini, P., & Zdziarski, A. A. 2007, ApJ, 657, 448
Ford, E. C., van der Klis, M., & Kaaret, P. 1998, ApJ, 498, L41
Frank, J., King, A. R., & Raine, D. J. 1985, Accretion Power in Astrophysics (Cambridge and New York: Cambridge Univ. Press)
Frontera, F., et al. 1997, A&AS, 122, 357
Galloway, D. K., Psaltis, D., Muno, M. P., & Chakrabarty, D. 2006, ApJ, 639, 1033
Gierliński, M., & Done, C. 2002, MNRAS, 337, 1373
Gottwald, M., et al. 1989, ApJ, 339, 1044
Haberl, F., & Titarchuk, L. 1995, A&A, 299, 414
Hasinger, G., & van der Klis, M. 1989, A&A, 225, 79
Homan, J., Kaplan, D. L., van den Berg, M., & Young, A. J. 2009, ApJ, 692, 73
Homan, J., et al. 2010, arXiv:1005.3210
Iaria, R., et al. 2005, A&A, 439, 575
Inogamov, N. A., & Sunyaev, R. A. 1999, Astron. Lett., 25, 269
Kluzniak, W., & Wilson, J. R. 1991, ApJ, 372, L87
Koyama, K., et al. 2007, PASJ, 59, 23
Levine, A. M., et al. 1996, ApJ, 469, L33
Lin, D., Remillard, R. A., & Homan, J. 2007, ApJ, 667, 1073
Lin, D., Remillard, R. A., & Homan, J. 2009, ApJ, 696, 1257
Madej, J., Joss, P. C., & Różańska, A. 2004, ApJ, 602, 904
McClintock, J. E., Narayan, R., & Shafee, R. 2007, arXiv:0707.4492
McClintock, J. E., et al. 2009, ApJ, 698, 1398
Miller, J. M. 2007, ARA&A, 45, 441
Mitsuda, K., et al. 1984, PASJ, 36, 741
Mitsuda, K., Inoue, H., Nakamura, N., & Tanaka, Y. 1989, PASJ, 41, 97
Mitsuda, K., et al. 2007, PASJ, 59, 1
Ng, C., et al. 2010, arXiv:1005.3755
Olive, J.-F., Barret, D., & Gierliński, M. 2003, ApJ, 583, 416
Oosterbroek, T., Barret, D., Guainazzi, M., & Ford, E. C. 2001, A&A, 366, 138
Özel, F. 2006, Nature, 441, 1115
Parmar, A. N., et al. 1997, A&AS, 122, 309
Parmar, A. N., et al. 1999, A&AS, 136, 407
Piraino, S., et al. 2007, A&A, 471, L17
Popham, R., & Sunyaev, R. 2001, ApJ, 547, 355
Reis, R. C., Fabian, A. C., & Young, A. J. 2009, MNRAS, 399, L1
Remillard, R. A., & McClintock, J. E. 2006, ARA&A, 44, 49
Rutledge, R. E., Bildsten, L., Brown, E. F., Pavlov, G. G., & Zavlin, V. E. 1999, ApJ, 514, 945
Shafee, R., et al. 2006, ApJ, 636, L113
Shimura, T., & Takahara, F. 1995, ApJ, 445, 780
Steiner, J. F., Narayan, R., McClintock, J. E., & Ebisawa, K. 2009, PASP, 121, 1279
Takahashi, T., et al. 2007, PASJ, 59, 35
Titarchuk, L. 1994, ApJ, 434, 570
van der Klis, M. 2006, in Compact Stellar X-ray Sources, ed. W. Lewin & M. van der Klis (Cambridge: Cambridge Univ. Press), 39
White, N. E., Stella, L., & Parmar, A. N. 1988, ApJ, 324, 363